Controlling the 3-D Morphology of Ni-Fe-Based Nanocatalysts for the Oxygen Evolution Reaction

Ryan H. Manso,[1,†] Prashant Acharya,[2,†] Shiqing Deng,[3,4†] Cameron C. Crane;[1] Benjamin Reinhart,[5] Sungsik Lee,[5] Xiao Tong,[6] Dmytro Nykypanchuk,[6] Jing Zhu,[4] Yimei Zhu,[3] Lauren F. Greenlee,[2,*] and Jingyi Chen[1,*]

[1]Department of Chemistry and Biochemistry, University of Arkansas, Fayetteville, AR 72701, USA

[2]Ralph E. Martin Department of Chemical Engineering, University of Arkansas, Fayetteville, AR 72701, USA

[3]Condensed Matter Physics and Materials Science Department, Brookhaven National Laboratory, Upton, NY 11973, USA

[4]School of Materials Science and Engineering, Tsinghua University, Beijing 100084, P. R. China

[5]Advanced Photon Source, Argonne National Laboratory, Lemont, IL 60439, USA

[6]Center for Functional Nanomaterials, Brookhaven National Laboratory, Upton, NY 11973, USA

[†]These authors contributed to this work equally.

[*]Corresponding authors: chenj@uark.edu (synthesis, characterization) and greenlee@uark.edu (electrocatalysis, characterization)

Abstract: Controlling the 3-D morphology of nanocatalysts is one of the underexplored but important approaches for improving the sluggish kinetics of oxygen evolution reaction (OER) in water electrolysis. This work reports a scalable, oil-based method based on thermal decomposition of organometallic complexes to yield highly uniform Ni-Fe-based nanocatalysts with well-defined morphology (i.e., Ni-Fe core-shell, Ni/Fe alloy, and Fe-Ni core-shell). Transmission electron microscopy reveals their morphology and composition to be NiO_x-FeO_x/NiO_x core-mixed shell, NiO_x/FeO_x alloy, and FeO_x-NiO_x core-shell. X-ray techniques resolve the electronic structures of the bulk and are supported by electron energy loss spectroscopy analysis of individual nanoparticles. These results suggest the crystal structure of Ni is most likely to contain α-$Ni(OH)_2$ and that the chemical environment of Fe is variable, depending on the morphology of the nanoparticle. The Ni diffusion from the amorphous Ni-based core to the iron oxide shell makes the NiO_x-NiO_x/FeO_x core-mixed shell structure the most active and the most stable nanocatalyst, which outperforms the comparison NiO_x/FeO_x alloy nanoparticles expected to be active for OER. This study suggests that the chemical environment of the mixed NiO_x/FeO_x alloy composition is important to achieve high electrocatalytic activity for OER and that the 3-D morphology plays a key role in optimization of the electrocatalytic activity and stability of the nanocatalyst for OER.

Introduction

Water electrolysis can be employed to produce hydrogen and oxygen as an alternative, more environmentally friendly means to generate clean renewable fuels.[1-2] In principle, water splitting is straightforward, separating into two half reactions on the cathode (hydrogen evolution reaction, HER) and anode (oxygen evolution reaction, OER), but the efficiency of the overall reaction remains limited. One of the major obstacles is the slow kinetics of the four-electron OER, which requires a much greater applied potential than the thermodynamic standard potential.[1] Finding catalytic materials to lower the amount of potential applied above the thermodynamic requirement (i.e., overpotential) remains a necessary task to allow potential viable commercialization of water electrolysis. Electrocatalysts based on noble metals such as Pt, Ru, Ir, and their oxides have been extensively investigated for OER due to appreciable activity and relatively high stability.[3-4] Compared to Pt, Ru, and Ir, their oxides were better catalysts with relatively low overpotentials, and thus RuO_x and IrO_x have been recommended as benchmarks in the development of active electrocatalysts for OER.[5-7] Despite their superior performance, the high cost of these scarce materials makes their choice difficult for large-scale industrial use. It is a critical need to search for inexpensive materials with high catalytic performance for OER to enable practical use in water electrolyzers.

The earth-abundant 3-*d* transition metal-based materials such as Mn, Fe, Co, and Ni oxides and hydroxides have emerged as promising catalyst candidates for OER under alkaline conditions.[8-12] Among these low-cost oxides and hydroxides, the Ni-Fe-based materials are among the most active catalysts, with catalytic activity for OER comparable to that of RuO_x and IrO_x.[13-15] Early studies on Ni-based alkaline batteries found that the presence of Fe could lower the OER overpotential on Ni-based electrodes.[16-17] In the 1980s, Corrigan first reported that the synergistic

effects of Fe and Ni on OER activity were the result of a Ni-Fe hydrous oxide composite with markedly different electrochemical properties compared to either monometallic material alone.[18] Since then, mixed Ni-Fe-based thin films have been extensively investigated through electrochemical methods,[19-25] *in situ* spectroscopic tools (e.g., Mössbauer spectroscopy,[26-28] Raman spectroscopy,[29-31] and x-ray absorption spectroscopy[32-39]) and density functional theory[36, 40-42] in an effort to understand reaction mechanisms and elucidate structure-activity relationships. The early study by Corrigan indicated that coprecipitating as little as 0.01% Fe could significantly lower the overpotential for OER.[18] Later, it was confirmed by other groups that Fe impurities in the electrolyte could substantially improve the OER activity of Ni-only materials.[19, 36] The optimal activity varied with the Fe composition in the films, with some studies showing similar performance in the range between 10-50%[18, 29] and others indicating 25% to be the optimum.[19-20] The discrepancy in optimal composition for improved OER activity may be due to the difference in the preparation methods and the resulting structures of these mixed Ni-Fe-based thin films. The commonly-used electrodeposition usually generates layered hydroxide structures, while other synthesis methods can produce different Ni-Fe-based structures. For example, thermal annealing generated a Fe_3O_4-based spinel structure hosted with Ni substitution, forming $NiFe_2O_4$,[34] while an aerosol-spray-assisted approach produced Ni-Fe-based amorphous materials.[43]

Since Ni-Fe-based materials appear to be one of the most active catalysts for OER in these thin film studies, progress has been recently made to reduce the dimension of these active Ni-Fe-based materials for improved OER activity. For example, single-layer nanosheets generated by liquid phase exfoliation of the layered double hydroxides exhibited significantly higher OER activity than their bulk counterparts.[44] More recent studies by *in situ* electrochemical atomic force microscopy illustrated the structural dynamics of these nanosheets under electrochemical

conditions.[45-46] On the other hand, nanoscale spinel-type Ni-Fe based oxides were synthesized by a solvothermal method and showed that the $Ni_xFe_{3-x}O_4$/Ni nanocomposite with an *x* value of ~0.36 exhibited the most superior activity for OER.[47] While nanocatalysts show promise to improve OER activity, little effort has been made to explore the morphological effects on the electrocatalytic performance of Ni-Fe-based nanocatalysts. Our previous multistep aqueous-based synthesis of Ni-Fe-based nanocatalysts demonstrated that a core-shell morphology having a $Fe/Fe(OH)_3$ core and a $Fe_xNi_{1-x}(OH)_2$ shell exhibited a superior OER activity.[48] In this work, we developed a scalable, oil-based synthesis approach based on thermal decomposition of organometallic complexes that enables manipulation of both the morphology and crystalline phase of the Ni-Fe nanocatalysts. Highly uniform Ni-Fe-based nanostructures with different morphologies (i.e., core-shell and alloy) were synthesized *via* either sequential or simultaneous injection. The uniform nanostructures enabled us to use transmission electron microscopy (TEM) for in-depth structural and electronic characterization of a single particle. Together with the x-ray methods on the bulk sample, we elucidate the morphology, composition, and structure of individual particles for each of these nanostructures in detail. We then evaluate the OER performance for these well-defined, Ni-Fe-based nanostructures with Ni and Fe alone nanoparticles. This study allows us to establish a fundamental understanding of as-synthesized morphological, compositional, and structural influences on the electrocatalytic activity of Ni-Fe-based nanocatalysts for OER.

Results and Discussion

Three Ni-Fe-based nanostructures with different morphologies were designed and synthesized for this study and included Ni-Fe-based core-shell, Ni-Fe-based alloy, and Fe-Ni-based core-shell. Nanostructure synthesis was achieved through solution-based thermal decomposition of organometallic complexes in high-boiling-temperature organic solvent. Programmable

temperature control was used to improve the uniformity of the resulting nanoparticles. The core-shell structures were synthesized using a two-step procedure with the first step to synthesize the cores, followed by the second step to coat the cores with the shells. The alloy structures were prepared in a one-step synthesis by simultaneously injecting both precursors into the solvent. During synthesis, the nanoparticles are oxidized when exposed to the ambient atmosphere, and thus we denote the resulting Ni-Fe-based nanostructures as nickel oxides (NiO_x) and iron oxides (FeO_x). After synthesis, the nanoparticles were transferred from the organic phase into aqueous solution through ligand exchange process using polyethylene glycol terminated with carboxylic acid (PEG-COOH). The overall reaction yield is ~70% and the estimated cost for the synthesis was listed in **Table S1**. The analytical TEM, XPS, XRD, and XAS, as well as the electrochemical characterization were performed on the nanoparticles with PEG-COOH as surface ligands.

NiO_x-FeO_x core-shell nanoparticles were synthesized by thermally decomposing $Fe(CO)_5$ complex in the presence of preformed NiO_x seeds. **Figure 1A** displays a representative TEM image of the reaction product, indicating a core-shell morphology of the nanoparticles. These nanoparticles are relatively uniform with an overall diameter of 16.8 ± 2.0 nm. The size of the core NiO_x nanoparticles is 12.4 ± 0.6 nm (**Figure S1**), and the shell thickness of the core-shell nanoparticles is estimated to be ~2.2 nm. The x-ray photoelectron spectroscopy (XPS) study indicates that the binding energies of Fe $2p_{3/2}$ and Ni $2p_{3/2}$ of the core-shell nanoparticles are at 711.5 eV and ~856.4 eV, respectively, confirming the formation of FeO_x and NiO_x (**Figure S2**).

Further characterization of an individual nanoparticle using high-resolution transmission electron microscopy (HRTEM) and high-angle annular dark-field-scanning transmission electron microscopy (HAADF-STEM) imaging clearly showed a core-shell morphology, but rather poor crystallinity (**Figure 1, B and C**). The corresponding electron energy-loss spectroscopy (EELS)

mapping of the individual nanoparticle in the HAADF-STEM image reveals elemental distribution of a Ni-Fe core-shell structure (**Figure 1D**). Quantitative analysis of the EELS mapping reveals that the overall atomic ratio of Ni to Fe for individual NiO_x-NiO_x/FeO_x core-mixed shell nanoparticles is around 1.36 to 1, close to the 1:1 ratio obtained through inductively coupled plasma mass spectrometry (ICP-MS) of the sample. It is worth noting that Ni is not confined in the core but diffuses into the shell. The composition of the shell was analyzed by extracting the signals of Ni and Fe in the ring region, where the shell is projected in the 2-D EELS map (**Figure S3**). The quantitative analysis indicates that a 0.39:1 atomic ratio of Ni:Fe is present in the shell corresponding to atomic percent of 28% Ni and 72% Fe. Therefore, the NiO_x-FeO_x core-shell nanoparticles are actually made of a NiO_x core and a NiO_x/FeO_x mixed shell, denoted as NiO_x-NiO_x/FeO_x core-mixed shell structures.

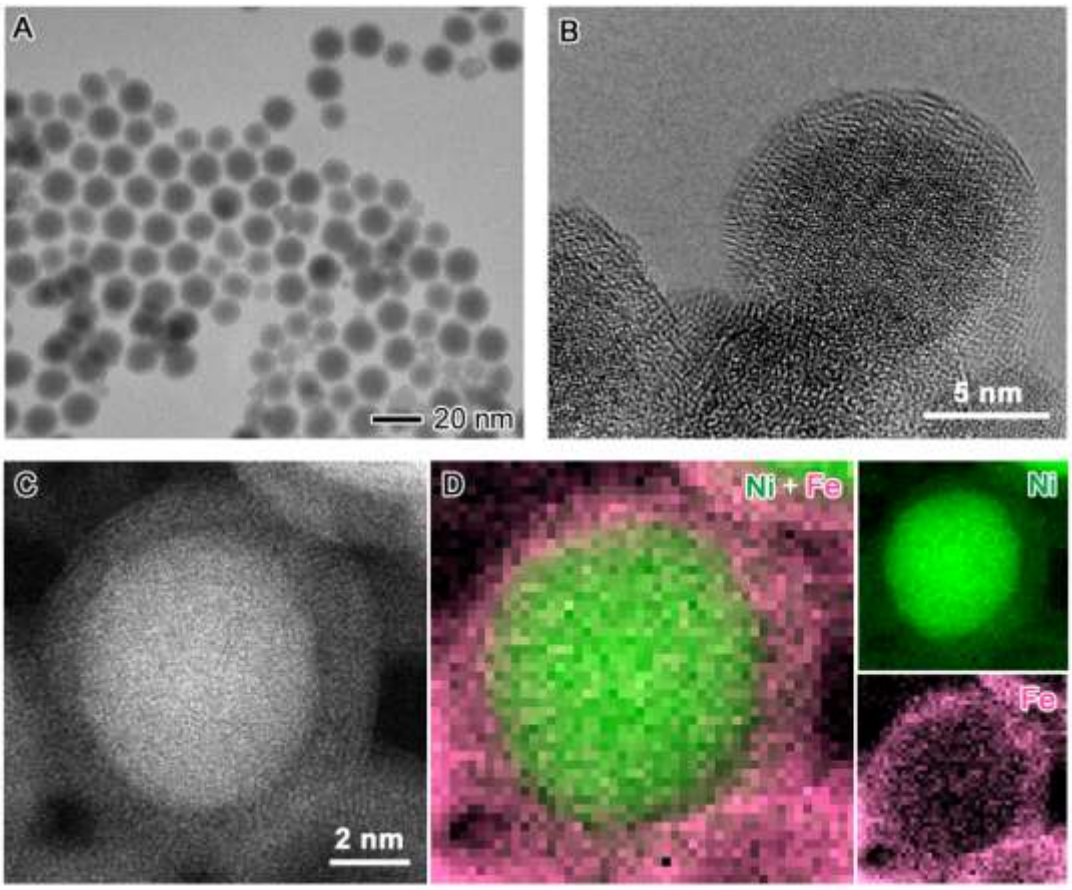

Figure 1. Electron microscopy characterization of NiO_x-NiO_x/FeO_x core-mixed shell nanoparticles: (A) TEM image overview of the nanoparticles with an average diameter of 16.8 ± 2.0 nm; (B,C) HRTEM and HAADF-STEM images displaying a representative nanoparticle in (A) which is mostly amorphous; (D) EELS mapping of the nanoparticle in (C) with Ni (green), Fe (pink), and Ni-Fe overlaid maps indicating a NiO_x-NiO_x/FeO_x core-mixed shell morphology. The Ni/Fe atomic ratio of the shell is 0.39:1.

NiO_x/FeO_x alloy nanoparticles were prepared using a similar procedure to that of NiO_x preparation except that the reactant $Ni(acac)_2$ alone in the NiO_x synthesis was replaced by the mixture of $Ni(acac)_2$ and $Fe(acac)_3$ at a 1:1 molar ratio in the alloy nanoparticle synthesis. From the TEM image in **Figure 2A,** the alloy nanoparticles appear to be more or less spherical in shape but are less uniform and slightly smaller compared to NiO_x nanoparticles. The average size of the alloy nanoparticles is 9.4 ± 1.7 nm. HRTEM image clearly shows the lattice fringes of an alloy nanoparticle, indicating good crystallinity (**Figure 2B**). No obvious contrast difference is observed in the HAADF-STEM image, suggesting homogenous distributions of Ni and Fe in a single, or similar density, phase(s) across the entire nanoparticle (**Figure 2C**). The corresponding EELS mapping agrees with the observations made from HAADF-STEM image contrast, wherein Ni and Fe are co-localized evenly across the nanoparticle, indicating an alloy composition (**Figure 2D**). The XPS spectra of the NiO_x/FeO_x nanoparticles in **Figure S2** indicate that the peak position of the Fe $2p_{3/2}$ and Ni $2p_{3/2}$ binding energies are 712.1 eV and 857.1 eV, respectively, confirming the oxide formation. The NiO_x/FeO_x mixed oxides have higher binding energies than FeO_x (710.7 eV for Fe $2p_{3/2}$) or NiO_x (856.6 eV for Ni $2p_{3/2}$). Quantitative analysis of the EELS spectra indicates that the Ni/Fe atomic ratio of individual particles is ~0.8, which is close to ICP-MS analysis, showing the overall Ni/Fe atomic ratio of the sample to be 1:1.

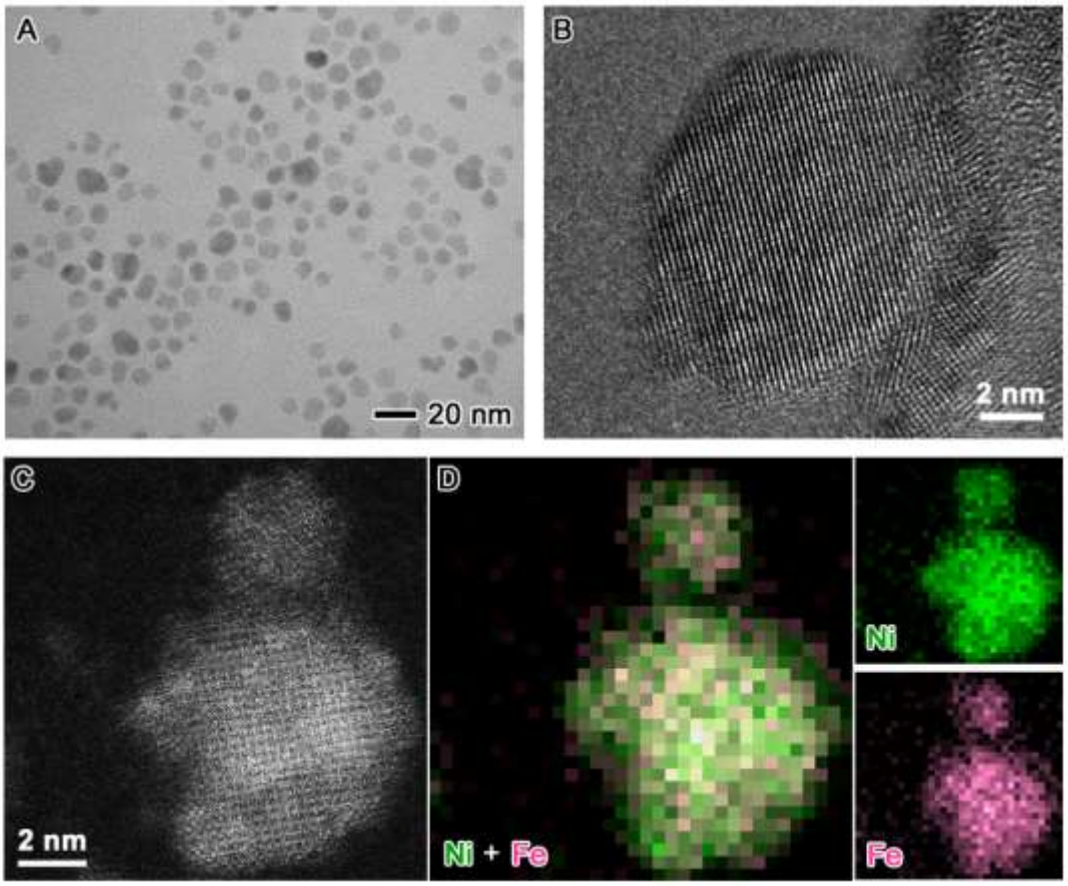

Figure 2. Electron microscopy characterization of NiO_x/FeO_x alloy nanoparticles: (A) TEM image overview of the nanoparticles with an average diameter of 9.4 ± 1.7 nm. (B,C) HRTEM and HAADF-STEM images displaying a representative nanoparticle in (A) which is crystalline; (D) EELS mapping of the nanoparticle in (C) with Ni (green), Fe (pink), and Ni-Fe overlaid maps indicating a NiO_x/FeO_x alloy composition.

FeO_x-NiO_x core-shell nanoparticles were also synthesized using a two-step procedure by first generating the FeO_x nanoparticles and then coating them with NiO_x shells. The FeO_x nanoparticles were prepared by thermally decomposing $Fe(acac)_3$ in a mixture of dibenzyl ether and oleylamine. These FeO_x nanoparticles are spherical in shape with an average diameter of 9.0 ± 1.7 nm according to TEM imaging (**Figure S4**). The coating process was performed using thermal decomposition of bis(1,5-cyclooctadienenickel(0) ($Ni(COD)_2$) in the presence of the FeO_x nanoparticles. After coating with the Ni shells, the FeO_x-NiO_x core-shell nanoparticles have an

average diameter of 9.8 ± 1.6 nm, as shown in **Figure 3A**. The shell thickness is estimated to be ~0.4 nm. HRTEM result suggests that the nanoparticles exhibit a good crystallinity of the FeO_x core, which is covered with an amorphous NiO_x shell (**Figure 3B**). In the HAADF-STEM image, the contrast does not show an obvious core-shell structure (**Figure 3C**); however, the EELS mapping of an individual nanoparticle indicates that the Ni signal covers a slightly larger area, as compared to the Fe signal (**Figure 3D**). The Ni/Fe ratio of the entire nanoparticle was calculated to be around 0.078:1, corresponding to atomic percent 7.2% Ni, which is much less than that measured from ICP-MS (18.0% Ni). This difference could be attributed to the presence of pure Ni, possibly from leached Ni or from homogenous, nucleated Ni. The XPS spectra of the FeO_x-NiO_x core-shell nanoparticles in **Figure S2** confirm the oxide composition with the peak positions of the Fe $2p_{3/2}$ and Ni $2p_{3/2}$ binding energies to be 710.7 eV and 855.5 eV, respectively.

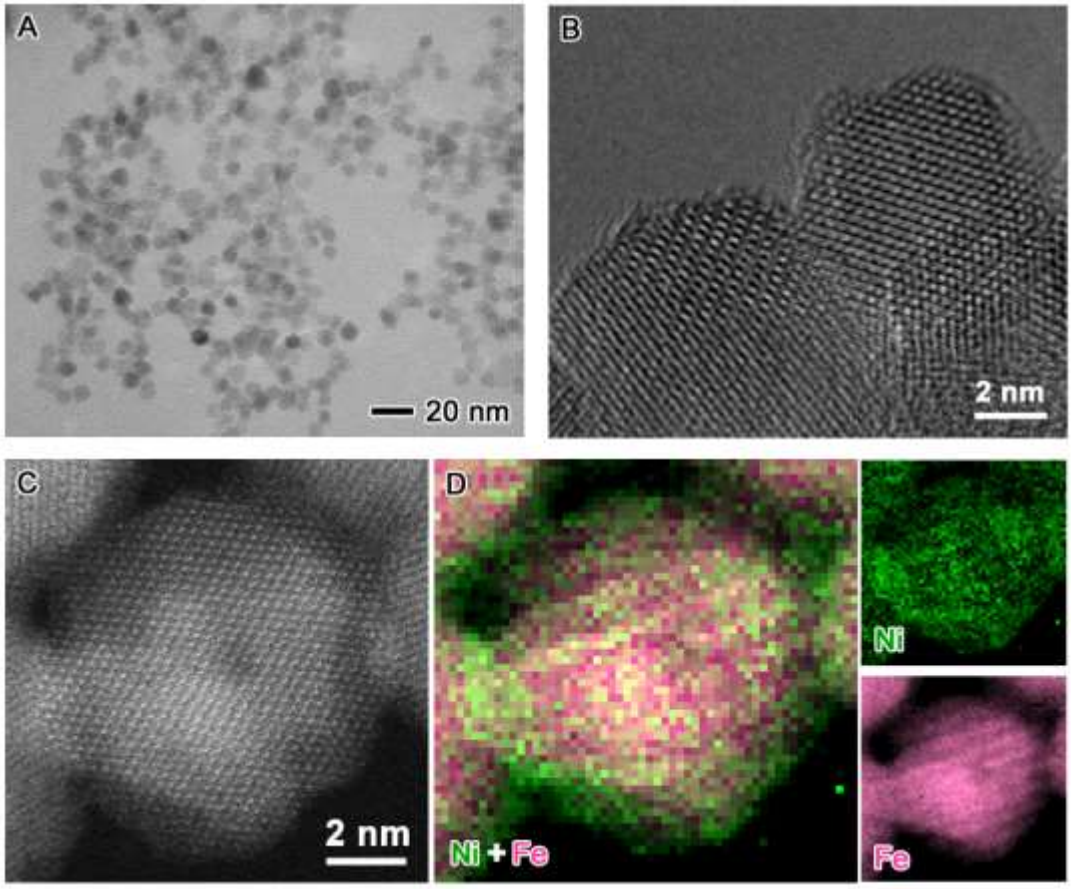

Figure 3. Electron microscopy characterization of FeO_x-NiO_x core-shell nanoparticles: (A) TEM image overview of the nanoparticles with an average diameter of 9.8 ± 1.6 nm; (B,C) HRTEM and HAADF-STEM images displaying a representative nanoparticle in (A) with a crystalline core and a thin amorphous shell; (D) EELS mapping of the nanoparticle in (C) with Ni (green), Fe (pink), and Ni-Fe overlaid maps, confirming the core-shell structure.

The crystal structures of these Ni-Fe-based nanoparticles were analyzed by x-ray powder diffraction (XRD) on the bulk samples, as shown in **Figure 4**. The XRD pattern of the NiO_x nanoparticles indicates three broad peaks at 30.4°, 47.0°, and 60.1°, which can be indexed to α-$Ni(OH)_2$ with Ni(II) valence.[49-50] The weak and broad XRD signals are ascribed to the lack of long-range order in the α-$Ni(OH)_2$ crystal structure. According to the XRD pattern, the FeO_x nanoparticles could be composed of γ-Fe_2O_3 with Fe(III) valance and/or Fe_3O_4 with mixed valence of Fe(II) and Fe(III). Since $Fe(acac)_3$ with Fe^{3+} was used as the precursor, the FeO_x nanoparticles are likely to be γ-Fe_2O_3; however, we cannot rule out the possibility of the presence of Fe(II) in the form of Fe_3O_4 because the reaction was carried out under a reducing environment with the presence of oleylamine.[51] The XRD pattern of the NiO_x-NiO_x/FeO_x core-mixed shell nanoparticles is essentially the same as that of NiO_x with three broad peaks at 30.4°, 47.0°, and 60.1°, suggesting that the mixed NiO_x/FeO_x shell is largely amorphous consistent with HRTEM result in Figure 1B. According to our previous study, the thermal decomposition of $Fe(CO)_5$ at the early stage when reaction temperature was relatively low (180 °C) yielded mostly amorphous FeO_x; if any crystallinity is present, it should be below the detection limit of XRD (< 2%).[52] Based on these results, it is suggested that the core-shell nanoparticles are made of α-$Ni(OH)_2$ and Fe_3O_4. For the NiO_x/FeO_x alloy nanoparticles, the XRD pattern appears to be a mixture of α-$Ni(OH)_2$ and iron oxide(s). Similar to the FeO_x nanoparticles, the FeO_x in the alloy is likely to be γ-Fe_2O_3 due to the same precursor $Fe(acac)_3$ used in the synthesis. Compared to that of the FeO_x nanoparticles, the XRD pattern of FeO_x-NiO_x core-shell nanoparticles exhibits an additional broad peak at 47.0° that

can be assigned to α-Ni(OH)$_2$. The weak α-Ni(OH)$_2$ is due to a small amount (~10 atomic%) of Ni in the FeO_x-NiO_x core-shell nanoparticles. The presence of α-Ni(OH)$_2$ as the primary phase for Ni atoms is promising for the OER because this more disordered phase of nickel hydroxide is now known to be the more active phase for alkaline OER.[19] The presence of peaks for iron oxide phases does suggest that at least some, or perhaps all, of the Fe atoms are present in a separate oxide phase in the as-synthesized nanoparticles. However, it is also possible that some of the Fe and Ni atoms are present in a combined hydroxide phase, as has been suggested for other Fe-Ni hydroxide/oxide materials.[22, 36]

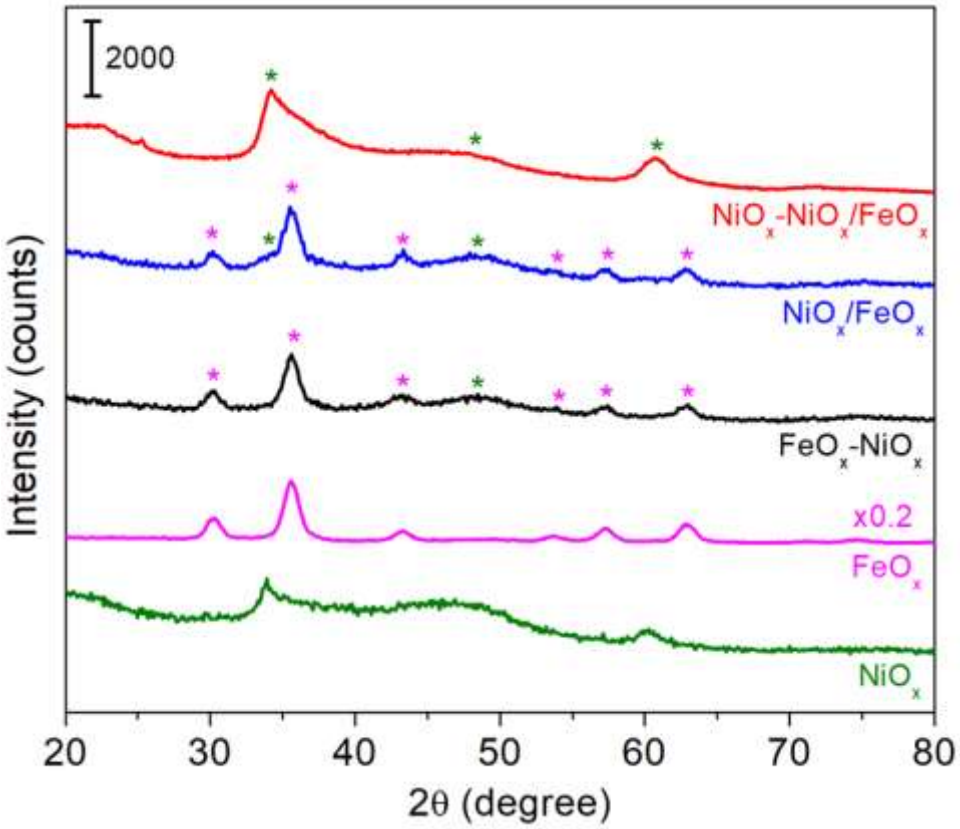

Figure 4. XRD patterns of different nanoparticle samples: NiO_x-NiO_x/FeO_x core-mixed shell (red), NiO_x/FeO_x alloy (blue), FeO_x-NiO_x core-shell (black), FeO_x (pink), and NiO_x (green). The peaks assigned to α-Ni(OH)$_2$ are labelled by green stars while the peaks indexed to Fe_3O_4 or γ-Fe_2O_3 are labelled by pink stars.

Ex situ XAS was performed on this series of nanocatalysts to examine the collective composition and structure of each nanocatalyst. The spectra for Fe are plotted in **Figure 5**, supplemented with a full set of Fe standard spectra plotted in **Figure S5**. The spectral shapes of the Fe K-edge for FeO_x nanoparticles, FeO_x-NiO_x core-shell nanoparticles, and the NiO_x/FeO_x alloy nanoparticles appear quite similar. However, at the white line, the peak intensity is noticeably different for the three samples, and the peak position of the edge is shifted slightly to higher eV for FeO_x and NiO_x/FeO_x. When comparing across different sample morphologies and metal compositions, an increase in peak height can suggest an increase in order or crystallinity, while a shift to higher eV most likely suggests a larger portion of the Fe atoms are in a higher oxidation state. These results support HRTEM and XRD results, where NiO_x/FeO_x and FeO_x-NiO_x nanoparticles were both found to be more crystalline than the NiO_x-NiO_x/FeO_x core-mixed shell nanoparticle sample. The shift to slightly higher eV for FeO_x suggests that more of the Fe atoms are likely to be in the 3+ oxidation state, rather than in the 2+ oxidation state, a conclusion that is also supported by the discussion above and the use of a Fe^{3+} precursor during synthesis. Similarly, the NiO_x/FeO_x alloy nanoparticle sample, also synthesized from the Fe^{3+} precursor, has an edge position that is shifted slightly to higher eV, as compared to the FeO_x-NiO_x core-shell nanoparticle sample. This result could be explained by the synthesis process in which the FeO_x nanoparticles from the same synthesis were used as seeds for core-shell nanoparticle growth. Even though the FeO_x-NiO_x core-shell nanoparticles were synthesized starting with the FeO_x nanoparticles, which would suggest that that Fe K-edge position should also be shifted to higher eV and match that of the NiO_x/FeO_x and FeO_x samples, the edge is in fact positioned at a slightly lower eV. This result is consistent with the EELS Fe $L_{2,3}$-edge results in **Figure 7** and suggests that the Fe atoms were in a more electron-rich chemical environment in this sample. The pre-edge features of all three

samples are quite similar in shape and position and align most closely with the $NiFe_2O_4$ pre-edge position, albeit with a lower pre-edge intensity. The lower pre-edge intensity suggests an octahedral coordination environment, and the lower pre-edge intensity combined with the lower eV edge position suggest an iron phase that has Fe(II) and Fe(III) species. While the edge is not shifted fully to the lower eV position of the Fe_3O_4 reference material, the slight shift is suggestive of some of the Fe atoms having a lower oxidation state, similar to that of a Fe_3O_4-like phase, perhaps in combination with a Fe_2O_3-like phase. The minor shift suggests a small contribution of more electron-rich Fe atoms to the overall ensemble of Fe in the nanoparticles.

For the NiO_x-NiO_x/FeO_x core-mixed shell nanoparticle sample, the Fe K-edge spectrum exhibited features that are quite different from that of NiO_x/FeO_x alloy or FeO_x-NiO_x core-shell nanoparticles. This result may potentially be in part because the $Fe(CO)_5$ precursor was used in place of $Fe(acac)_3$. However, the result may also be a result of the different core-shell morphology that was formed and the presence of Fe in the iron oxide shell. The edge peak is broad and has a decreased intensity, as compared to the other samples. This result suggests a more disordered structure to the nanoparticles, as well as a population of oxidation states within the nanoparticle. By comparing with spectra of the standard samples, the Fe in this sample is likely to be a mixture of 2+/3+ state, which also agrees with the XRD results. The slightly higher intensity pre-edge suggests a distorted octahedral structure. This change in the pre-edge feature may be a result of the mixed metal oxide/hydroxide shell, where the presence of both metals in an oxide/hydroxide phase would likely cause distortions in the coordination chemistry of the Fe.

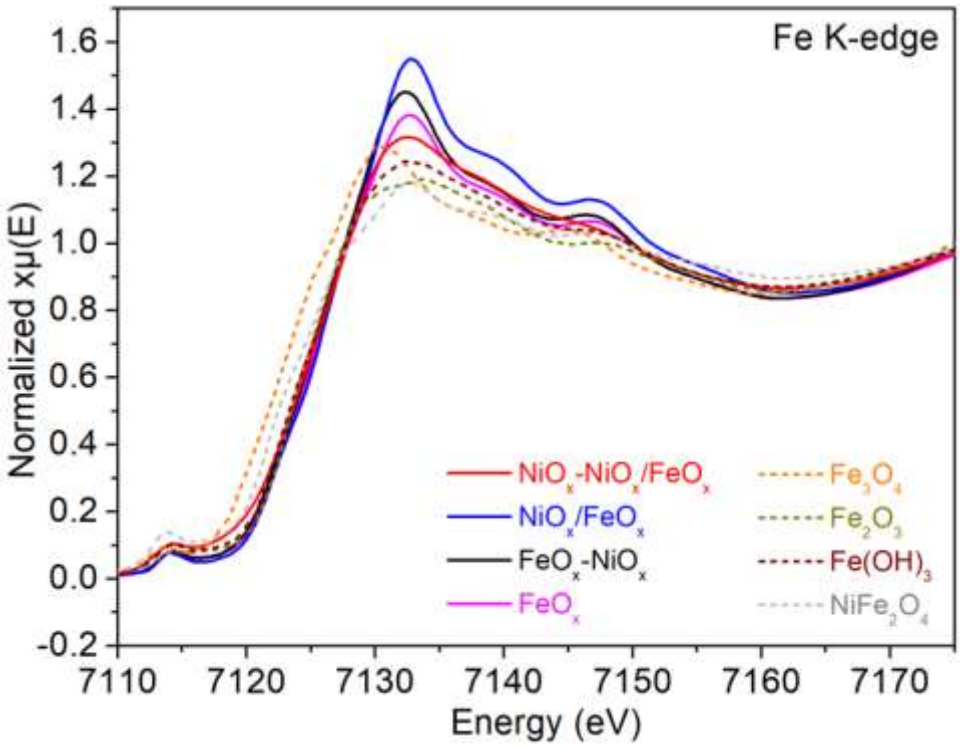

Figure 5. XAS spectra of Fe K-edge for the nanoparticle catalysts: NiO_x-NiO_x/FeO_x core-mixed shell (red), NiO_x/FeO_x alloy (blue), FeO_x-NiO_x core-shell (black), and FeO_x (pink). The XAS spectra of selected Fe bulk standards were plotted in dash curves: Fe_3O_4 (orange), Fe_2O_3 (dark yellow), $Fe(OH)_3$ (wine), and $NiFe_2O_4$ (grey).

The EXAFS region (**Figure S6**) suggests slight differences in Fe-O bond length in the first coordination sphere amongst the experimental samples, along with a shoulder around 1 Å, which is indicative of a contribution from iron hydroxide and similar to EXAFS spectra obtained for the Fe K edge of other $Fe_xNi_y(OH)_z$ materials.[36, 53] All experimental samples appear to have an Fe-O bond length that is slightly larger than the most relevant reference material, Fe_3O_4, and the NiO_x-NiO_x/FeO_x core-mixed shell nanoparticle sample resulted in a slightly larger bond length than the other experimental samples. The second coordination sphere metal-metal distances (Fe-O-Fe/Ni) also vary as a function of the different experimental samples and as compared to the reference materials. Generally, there appears to be more variability in the second coordination sphere than in the first coordination sphere, which may result from the influences of Fe-Ni substitution and

phase structural differences as a result of the different morphologies synthesized in nanoparticle form. The broad peak obtained for core-shell FeO_x-NiO_x is suggestive of the Fe_3O_4 reference material spectra,[54-56] with less well-defined peak separation within the second coordination sphere; this peak splitting is caused by the multiple chemical environments of the Fe atoms, and thus multiple Fe-O-Fe metal-metal distances, in the Fe_3O_4 crystal structure, nominally described as an Fe(II)/Fe(III) mixed oxidation state material. The peak of the second coordination sphere for FeO_x vs NiO_x/FeO_x is less broad and is positioned at shorter vs longer radial distance, respectively. The peak of the second coordination sphere for the core-mixed shell NiO_x-NiO_x/FeO_x has significantly lower peak intensity, suggesting structural disorder. The peak is also more narrow than those of the other experimental samples and is located at lower radial distance, as compared to NiO_x/FeO_x; lower radial distance is suggestive of a compressed Fe-O-M metal-metal bond distance.

The spectra for Ni are plotted in **Figure 6**, supplemented with a full set of Ni standard spectra plotted in **Figure S7**. The spectral shapes of the Ni K-edge for the NiO_x-NiO_x/FeO_x core-mixed shell nanoparticles and the NiO_x nanoparticles had nearly identical features in both the pre-edge and the white line edge. This result clearly indicates that the majority of the Ni atoms in the NiO_x-NiO_x/FeO_x core-mixed shell nanoparticles were in a chemical environment like that of the NiO_x nanoparticles, which is likely to be α-$Ni(OH)_2$, based on the XRD results. The NiO_x/FeO_x alloy nanoparticles resulted in a pre-edge shape and intensity that was quite similar to the NiO_x and NiO_x-NiO_x/FeO_x nanoparticles. All three samples have a pre-edge intensity that is higher than that of the α-$Ni(OH)_2$ reference material, suggesting that the Ni species of these three samples are in a distorted octahedral coordination geometry, rather than the octahedral geometry expected for α-$Ni(OH)_2$. In contrast, the pre-edge of the FeO_x-NiO_x core-shell nanoparticles matches the shape and intensity of α-$Ni(OH)_2$, suggesting the Ni atoms are in an octahedral coordination environment

typical of the alpha hydroxide phase. This conclusion is further supported by the similar white line edge position and peak intensity of the FeO_x-NiO_x core-shell nanoparticles, as compared to the α-$Ni(OH)_2$ reference material. Across the set of experimental samples, all of the samples displayed an edge position indicative of α-$Ni(OH)_2$, and thus, the Ni was likely in 2+ state.[22]

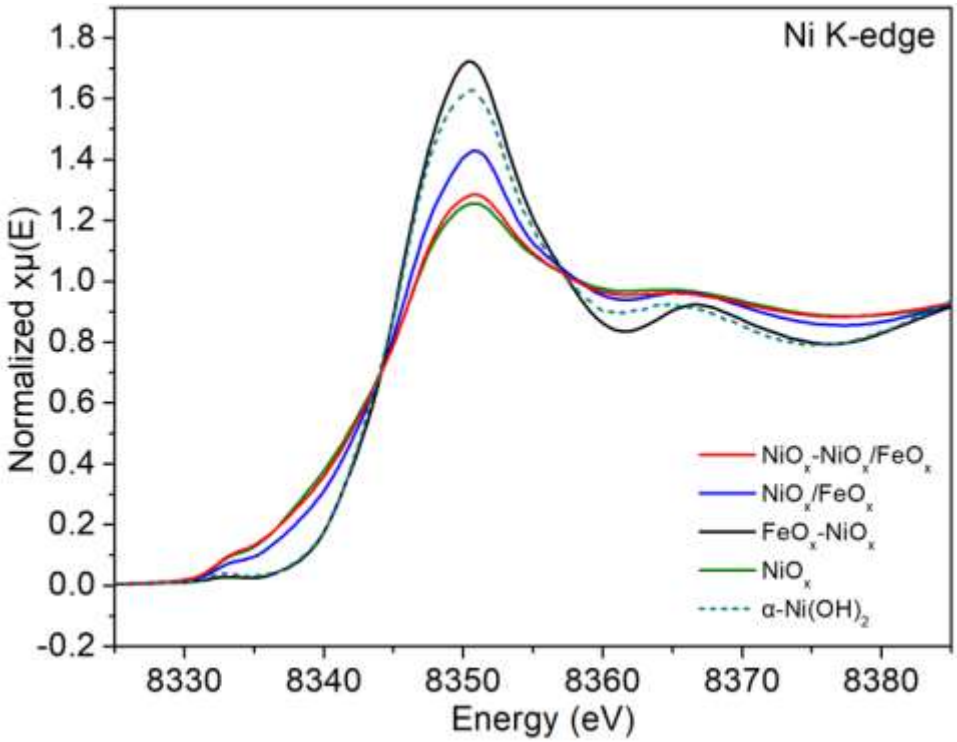

Figure 6. XAS spectra of Ni K-edge for the nanoparticle catalysts: NiO_x-NiO_x/FeO_x core-mixed shell (red), NiO_x/FeO_x alloy (blue), FeO_x-NiO_x core-shell (black), and NiO_x (green). The XAS spectrum of α-$Ni(OH)_2$ bulk standard was plotted in a dark green dash curve.

Similar to the results for the Fe K edge, the EXAFS region (**Figure S8**) suggests slight shifts in Ni-O first coordination sphere bond distances. However, the variability observed in the Fe EXAFS region for the second coordination sphere is not apparent in the Ni EXAFS region for the Ni second coordination sphere (Ni-O-Ni/Fe). This result may suggest that some of the differences observed in nanoparticle structure and, ultimately, electrochemical performance, are a result of differences in the chemical coordination environment of the Fe, more so than the Ni, species in

these nanoparticle materials. The shape and peak position of the second coordination sphere is quite similar to that of the α-$Ni(OH)_2$ reference material for all of the experimental samples.

Further analysis of EELS data from individual nanoparticles reveals the differences in local chemical states of Fe and Ni between the core and the shell in the core-shell structures and provides results that correspond well with XAS data on the bulk samples. **Figure 7** displays the EELS spectra of the Ni and Fe $L_{2,3}$-edges extracted from the center and the edge of the core-shell nanoparticles (i.e., NiO_x-NiO_x/FeO_x core-mixed shell and FeO_x-NiO_x core-shell) and the NiO_x/FeO_x alloy nanoparticle. No peak shifts for both the Fe and Ni $L_{2,3}$-edges were found for the alloy nanoparticles, suggesting the uniform chemical environment of both Fe and Ni across the nanoparticle, but shifts of the peak positions were observed in the EELS spectra for the core-shell structures. Based on the shift of the energy onset, the relative oxidation state,[57-58] coordination environment,[58-60] and electron density of elements in the center and the shell can be compared. The lower energy onset can correspond to a lower oxidation state or an electron rich state of the element due to the screening effect of outer-shell electrons.[61-62] For iron, a shift to lower energy onset may also suggest a shift in coordination from octahedral to tetrahedral. The direct comparison of the core and shell energy onset, however, is not straightforward because TEM is a 2-D projection of an object and thus each center spectrum contains the information of both the core and shell. Nonetheless, comparing the center and shell spectra, the energy shifts could provide evidence for local chemical environment changes of elements.

For NiO_x-NiO_x/FeO_x core-mixed shell nanoparticles, the energy positions of the Fe $L_{2,3}$-edges in the center and shell spectra are essentially the same because there is no Fe in the core and both spectra indicate the Fe in the shell. For Ni, however, the energy onset of the L_3 edge in the shell is 0.5 eV lower than that in the center. Although the center spectrum contains the Ni signal from

both the core and the shell, most of the Ni signal is contributed from the pure Ni core because the shell is very thin, with a thickness that is $1/8^{th}$ of the core diameter, and is composed of a mixture of Ni and Fe at an atomic ratio of 0.39/1. Prior work has shown that a shift to lower eV can be due to the presence of nickel metal rather than nickel oxide.[58] However, research has also shown that when metal atoms are incorporated into a nanostructured material, $L_{2,3}$ edge shifts may also occur and are thought, generally, to result from shifts in bi-metallic influences on coordination[60] and spin state.[63] It is unlikely that the Ni atoms in the shell of these nanoparticles experienced a full oxidation state change from Ni^{2+} to Ni^0; however, the Fe atoms present in the shell can contribute electron density to the Ni atoms. Thus, we might interpret the onset energy shift of the Ni in the shell as likely due to the contributions of electron transfer from surrounding Fe in the shell, which provide electron-rich Ni on the surface of the NiO_x-NiO_x/FeO_x core-mixed shell nanoparticles. This shift could also be a result of the strain effects; however, further analysis of the crystal structure difference at the core-shell interface is needed in order to determine the strain states.[64] Additional evidence for the proposed electron transfer or electron donation from Fe to Ni is supported by the Fe K edge EXAFS, where the smaller radial distance of the second coordination sphere suggests a compressed Fe-O-M bond distance and loss of electron density, along with the XPS results as shown in **Figure S2**. The binding energy of Fe 2p electrons for NiO_x-NiO_x/FeO_x increased by 0.8 eV compared to that for FeO_x while the binding energy of Ni 2p electrons for NiO_x-NiO_x/FeO_x decreased by 0.2 eV compared to that for NiO_x. These corroborative results suggest that electrons are preferentially transferred or donated from Fe to Ni in the shell of the NiO_x-NiO_x/FeO_x core-mixed shell nanostructures.

In contrast, for the FeO_x-NiO_x core-shell nanoparticles, no difference was observed in the peak position of the Ni L_3-edge in EELS spectra while a 0.5 eV shift to lower energy for the peak

position of the Fe L_3-edge was observed in the shell spectrum compared to the center spectrum. The shift to lower energy suggests the presence of Fe(II) species, which is supported by our previous analysis of the Fe K-edge spectra. This energy onset decrease in eV for the Fe at the interface of the core-shell nanoparticles could be attributed to the deposition of metallic Ni from the thermal decomposition of the Ni(0) organometallic complex thermal deposition, leading to an electron-rich environment for the surface Fe. The XPS data also indicates that Ni is more electron-rich in FeO_x-NiO_x core-shell nanoparticles than in NiO_x nanoparticles, which is likely due to the use of precursors with different valence (Ni^0 versus Ni^{2+}) in the corresponding synthesis. This result is consistent with XAS results that the Fe K edge of FeO_x-NiO_x core-shell is in fact positioned at a lower eV compared to FeO_x.

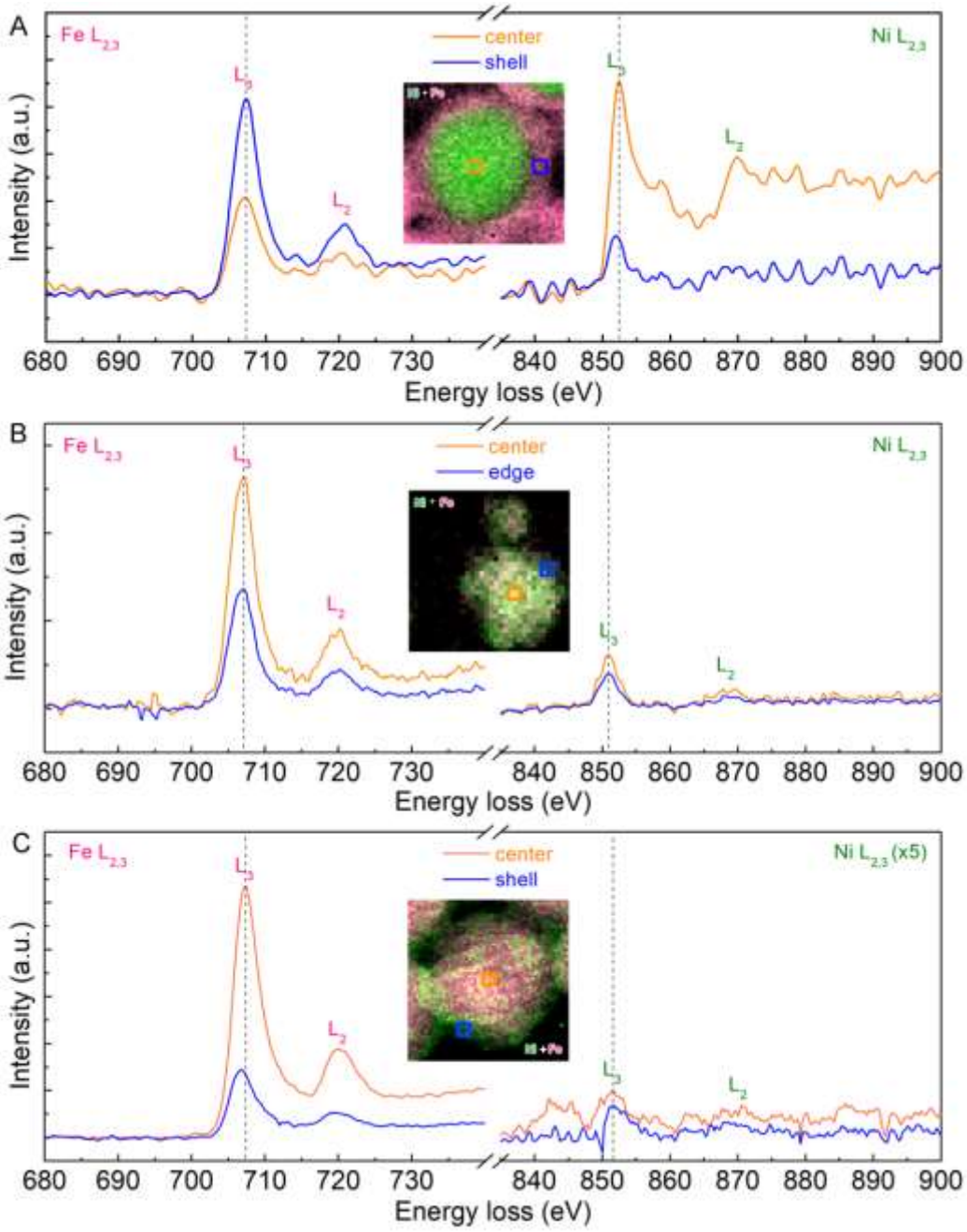

Figure 7. EELS spectra of Ni and Fe $L_{2,3}$-edges extracted from the center region (orange box) and the shell region (blue box) of each nanoparticle displayed in the inset of each panel: (A) NiO_x-NiO_x/FeO_x core-mixed shell nanoparticle showing that the energy positions of the Fe $L_{2,3}$-edges in the center and shell spectra were essentially the same while the energy onset of the Ni L_3 edge in the shell was 0.5 eV lower than that in the center. (B) NiO_x/FeO_x alloy nanoparticle indicating no peak shifts for both the Fe and Ni $L_{2,3}$-edges. (C) FeO_x-NiO_x core-shell nanoparticle showing that no difference was observed in the peak position of the Ni L_3-edge while a 0.5 eV shift to lower energy for the peak position of the Fe L_3-edge was observed in the shell spectrum compared to the center spectrum.

The three different morphologies of Ni-Fe-based nanostructures (i.e., NiO_x-NiO_x/FeO_x core-mixed shell, NiO_x-FeO_x alloy, and FeO_x-NiO_x core-shell) along with the controls (i.e., NiO_x and FeO_x) were evaluated for OER. The OER activity of the nanoparticles was assessed by their cyclic voltammetry (CV) profile in 1 M KOH. **Figure 8** shows the CV profile comparison of these nanocatalysts. The NiO_x-NiO_x/FeO_x core-mixed shell nanoparticles exhibited the best performance with the lowest onset potential, which reached the benchmark current density of 10 mA/cm^2 at 1.55 V vs RHE. Switching another water-soluble surface ligand such as PEG-NH_2 increased the onset potential by 60 mV (**Figure S9**). The NiO_x-FeO_x alloy nanoparticles had the second lowest onset potential and reached 10 mA/cm^2 at 1.60 V vs RHE. The remaining nanocatalysts were rather poor OER electrocatalysts, showing much higher onset potentials. The two bimetallic nanocatalysts (i.e., NiO_x-NiO_x/FeO_x core-mixed shell and NiO_x/FeO_x alloy) drastically outperformed the two monometallic nanocatalysts (i.e. NiO_x or FeO_x alone), which agrees with the literature reported on the thin film studies.[19, 22, 36, 65] Another bimetallic nanocatalyst (FeO_x-NiO_x core-shell) did not improve the onset potential compared to NiO_x or FeO_x, suggesting that the 3-D morphology has a significant influence on the electrocatalytic activity of the NiFe-based nanocatalysts. This result is also likely driven by the composition of the iron and nickel at the surface of the nanoparticles, where the atomic composition of Ni in the FeO_x-NiO_x core-shell nanoparticles was quite low (7.2%). We expect, based on prior literature,[19, 22, 29, 36, 65-66] that an Fe/Ni atomic ratio in the range of 20-80 to 50-50 will be the most active for OER. Interestingly, the NiO_x/FeO_x alloy nanoparticles fit this parameter range, but the NiO_x-NiO_x/FeO_x core-mixed shell nanoparticles do not fit this expectation, based on our compositional analysis from EELS. We thus attribute the OER activity of the NiO_x-NiO_x/FeO_x nanoparticles to the modified electronic structure of the Fe and Ni atoms in the mixed metal shell, where it appears

from EELS and XPS analysis that the Ni atoms are more electron rich, while the Fe atoms likely are donating electrons to the Ni atoms.

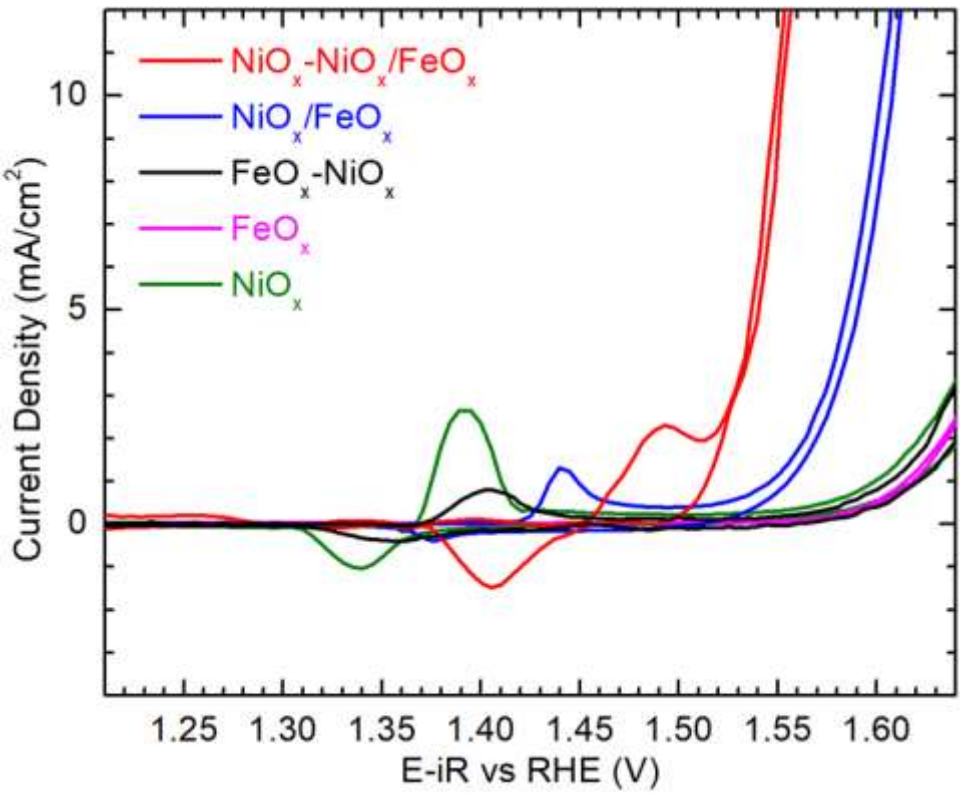

Figure 8. CV profiles of the nanoparticle catalysts obtained in 1 M KOH at a scan rate of 10 mV/s: NiO_x-NiO_x/FeO_x core-mixed shell (red), NiO_x/FeO_x alloy (blue), FeO_x-NiO_x core-shell (black), FeO_x (pink), and NiO_x (green).

The difference in 3-D morphology of these nanocatalysts also impacts the characteristic Ni redox peak in the region of 1.30 – 1.53 V of CV profiles. The NiO_x nanoparticles exhibited the largest area for the Ni redox peaks, which occurred at the lowest potential among all the nanocatalysts. As can be seen from the CV data, the height of the Ni redox peak does not necessarily correlate directly with OER activity; NiO_x alone is expected to have a distinct redox peak but low OER activity in purified alkaline electrolyte, as there are no Fe atoms present to enhance the OER reaction. The FeO_x-NiO_x core-shell nanocatalyst has a small characteristic Ni redox peak despite the presence of Ni; this small peak is likely an indication of the low Ni content

in these core-shell nanoparticles. NiO_x/FeO_x alloy nanoparticles had the second largest area for the Ni redox peak and a slight shift to higher voltage of the potential compared to NiO_x nanoparticles. Unlike NiO_x and NiO_x/FeO_x alloy nanoparticles, the NiO_x-NiO_x/FeO_x core-mixed shell nanoparticles had the highest voltage onset for the Ni redox peak, immediately before the onset potential of OER. The overall trend for the change of the characteristic Ni redox peaks agrees with previous studies,[19, 65] which concluded that incorporation of Fe in NiO_x thin films increases the Ni redox potential and decreases the area of the Ni redox peaks. Further analysis was performed to calculate the turnover frequency (TOF) based on the quantitative Ni in the samples, where the amount of Ni was estimated based on either the ICP-MS results or the integration of the redox wave (i.e., anodic wave) for each of the nanocatalysts. The TOF values for different nanocatalysts are listed in **Table S2**. For $TOF_{ICP\text{-}MS}$, the NiO_x-NiO_x/FeO_x core-mixed shell had the highest value of 1.175 s^{-1}, followed by NiO_x/FeO_x alloy with a value of 0.090 s^{-1}. The $TOF_{ICP\text{-}MS}$ values for NiO_x and FeO_x-NiO_x were 60-80 times lower at 0.006 s^{-1} and 0.003 s^{-1}, respectively. The $TOF_{redox\ wave}$ was also calculated with the assumptions of either 1 electron or 1.5 electron transfer per Ni atom.[67] The $TOF_{redox\ wave}$ values for all of the nanocatalysts were 2-5 times higher than those of the corresponding $TOF_{ICP\text{-}MS}$; however, the trend of both TOF values appeared to be the same in order of decreasing activity, with NiO_x-NiO_x/FeO_x core-mixed shell > NiO_x/FeO_x alloy > NiO_x ~FeO_x-NiO_x. The TOF values agreed well with the OER activity assessed based on the onset potential of the benchmark current density of 10 mA/cm^2.

In addition to the electrocatalytic activity, the stability of the nanocatalysts was measured by chronopotentiometry (CP) for 2 h in 1 M KOH, as shown in **Figure 9**. The degradation rate was calculated by taking the slope of potential over time for each curve corresponding to each nanocatalyst. The NiO_x-NiO_x/FeO_x core-mixed shell nanoparticles had the lowest degradation rate

of 5.4 mV/h, followed by NiO_x/FeO_x alloy nanoparticles at a rate of 10.9 mV/h. The FeO_x, NiO_x, and FeO_x-NiO_x had faster degradation rates at 24.1, 26.2, and 34.2 mV/h, respectively. The most active nanocatalyst (i.e. NiO_x-NiO_x/FeO_x core-mixed shell nanoparticles) was found to be the most stable electrocatalyst in this series. The NiO_x/FeO_x alloy was the second best electrocatalyst based on the assessment of both activity and stability. The NiO_x/FeO_x alloy nanoparticles has a mixed molar composition of ~0.8:1 (Ni:Fe) while the NiO_x-NiO_x/FeO_x core-mixed shell nanoparticles contains a pure NiO_x core and ~0.4:1 (Ni:Fe) mixed alloy shell, but the FeO_x-NiO_x core-shell appeared to be a pure NiO_x cluster shell (i.e., without any Fe included in the NiO_x structure). To our surprise, the NiO_x-NiO_x/FeO_x core-mixed shell nanoparticles, with half the amount of Ni in the shell compared to the NiO_x/FeO_x alloy nanoparticles, out-performed the NiO_x/FeO_x alloy nanoparticles in both activity and stability. Further adding a pure FeO_x shell increased the onset potential by 100 mV and thus reduced the electrocatalytic activity (**Figure S10**); and the FeO_x core-NiO_x/FeO_x mixed shell has similar activity as the NiO_x/FeO_x alloy with an onset potential at 1.64 V (**Figure S11**). These results suggest that the mixed NiO_x/FeO_x alloy composition is important to achieve high electrocatalytic activity for OER and the 3-D morphology plays a key role in optimization of the electrocatalytic activity and stability of the nanocatalyst for OER.

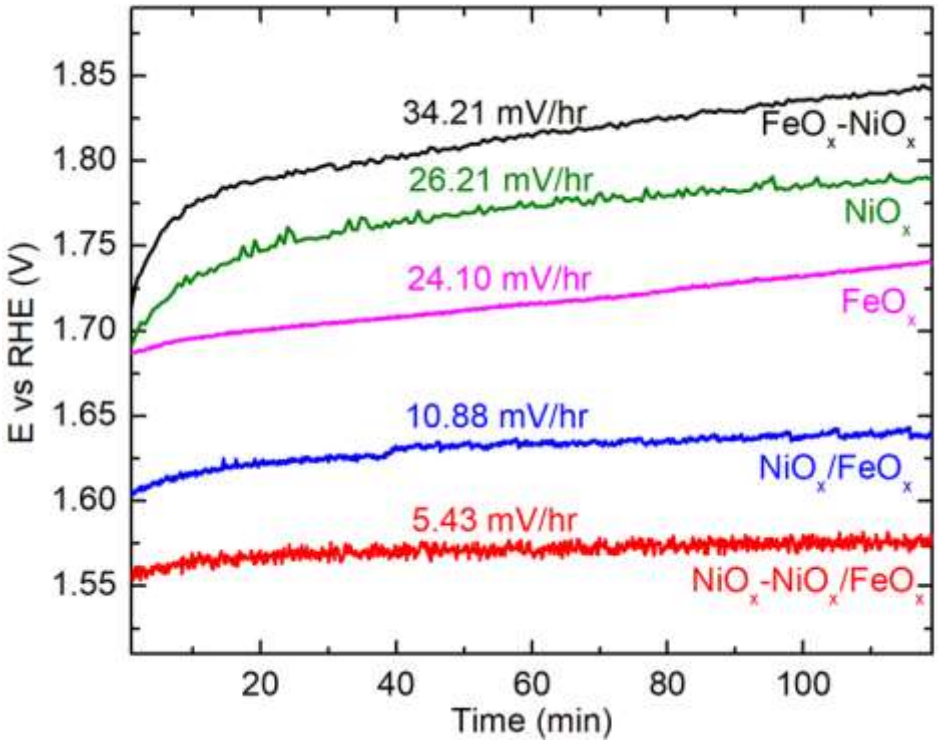

Figure 9. Chronopotentiometry (CP) of the nanocatalysts obtained in 1 M KOH at a current density of 10 mA/cm^2 for 2 h: NiO_x-NiO_x/FeO_x core-mixed shell (red), NiO_x/FeO_x alloy (blue), FeO_x-NiO_x core-shell (black), FeO_x (pink), and NiO_x (green).

Conclusion

In this study, we developed a scalable, oil-based synthesis based on thermal decomposition of organometallic complexes that could manipulate both the morphology and crystalline phase of the Ni-Fe-based nanocatalysts. Highly uniform Ni-Fe-based nanostructures with different morphologies (i.e., Ni-Fe core-shell, Ni/Fe alloy, and Fe-Ni core-shell) were synthesized *via* either sequential or simultaneous injection. TEM imaging revealed that the Ni-Fe core-shell was more complex due to the diffusion of Ni into the Fe shell, while the Ni-Fe alloy nanoparticle structure appeared to be a homogeneous mixture and the Fe-Ni core-shell structure contained an FeO_x core with NiO_x islands/thin shell. Coupled with x-ray characterization methods on the bulk and surface of the sample, we elucidate the morphology, composition, and structure of individual particles for each of these nanostructures to be NiO_x-NiO_x/FeO_x core-mixed shell, NiO_x/FeO_x alloy, and FeO_x-

NiO_x core-shell structures. The overpotentials of these nanocatalysts increased in the order of NiO_x-NiO_x/FeO_x core-mixed shell < NiO_x/FeO_x alloy < FeO_x-NiO_x core-shell structures ≈ NiO_x ≈ FeO_x. The TOF values obtained based on both ICP-MS and redox wave followed the same trend. These results suggested that the crystalline FeO_x core did not promote the catalytic activity of NiO_x in the FeO_x-NiO_x core-shell morphology, possibly due to the high crystallinity of FeO_x, which prevented Fe diffusion into the NiO_x shell. In contrast, the amorphous, disordered nature of the NiO_x core, which appears to be most similar to α-$Ni(OH)_2$, allowed the diffusion of Ni into the FeO_x for the NiO_x-NiO_x/FeO_x core-mixed shell nanoparticles. The resultant mixed metal hydroxide/oxide shell enabled the most active and stable nanocatalyst, which out-performed the comparison NiO_x/FeO_x alloy nanoparticles with a 1:1 composition expected to be active for OER. These findings highlight that not only the crystallinity, but also the 3-D morphology, phase, and chemical environment of both metal species, disorder, and composition, can significantly affect the electrocatalytic activity and stability of nanocatalysts for alkaline OER.

Experimental Methods

Synthesis of NiO_x-NiO_x/FeO_x Core-Mixed Shell Nanoparticles. The Ni-Fe core-shell nanoparticles were synthesized by a two-step procedure involving the synthesis of Ni core and following by coating the Ni core with Fe shell. In a typical synthesis, $Ni(acac)_2$ (51.5 mg, 0.2 mmol), 4 mL of octadecene (ODE), and 1 mL of oleylamine (OLAM) were added to a 3-neck, round bottom flask equipped with a condenser and a Schlenk line system. This reaction mixture was degassed for 10 min before 1mL of trioctylphosphine (TOP) was added to the reaction. Under the protection of argon, the reaction was heated to 220 ºC within 10 min and was held at 220 ºC for additional 20 min to allow the formation of Ni cores. The reaction was quenched by removing the flask from the heating mantle. After the reaction mixture was cooled to 50 ºC, the product was

transferred to a 50 mL centrifuge tube filled with 5 mL toluene and 20 mL of ethanol which was centrifuged at 8000 rcf for 5 min to remove excess reactants. The nanoparticle pellet was dispersed and purified using a mixture of 1:4 toluene and ethanol. The nanoparticles were dispersed in 6 mL of toluene.

For the Fe shelling procedure, 1.8 mL of the above Ni nanoparticles (~5 mg) was dried under a stream of argon in a 3-neck, round-bottom flask. Then, 200 μL of OLAM and 5 mL of ODE were added to the flask and the nanoparticles were dispersed in the mixture *via* sonication. To ensure a uniform coating, the reaction temperature was ramped using a step-wise procedure during the addition of Fe precursor. The temperature was first ramped to 100 ºC prior to the degassing of the reaction mixture. The temperature was then continued to ramp to 110 ºC and held for 10 min. Then, $Fe(CO)_5$ (20 μL, 0.15 mmol) was injected into the reaction using a gas-tight syringe. After adding the Fe precursor, the temperature was increased at a rate of 2.5 ºC/min until 200 ºC and the reaction was held at 200 ºC for 60 min. After the reaction was quenched and cooled to 50 ºC, the product was transferred to a 50 mL centrifuge tube filled with ethanol to 30 mL which was centrifuged at 8000 rcf for 5 min to remove excess reactants. The nanoparticle pellet was dispersed and purified using a mixture of 2:1 toluene and ethanol and collected by centrifuging at 2000 rcf for 10 min. The nanoparticles were dispersed in 2 mL of toluene.

Synthesis of Ni-Fe Alloyed Nanoparticles. Similar procedure was applied to the synthesis of alloyed nanoparticles as that for the Ni core synthesis except equimolar amounts of $Ni(acac)_2$ (25.7 mg, 0.1 mmol) and $Fe(acac)_3$ (26.5 mg, 0.1 mmol) were used in the reaction.

Synthesis of Fe-Ni Core-Shell Nanoparticles. The Fe-Ni core-shell nanoparticles were synthesized by a two-step procedure involving the synthesis of Fe core and following by coating the Fe core with Fe shell. The same reaction set up and heating procedure were used as that for the

Ni-Fe core-shell unless specified. In a typical synthesis, $Fe(acac)_2$ (530.0 mg, 1.5 mmol), 4 mL of .5 mL of dibenzyl ether (DBE), and 7.5 mL of oleylamine (OLAM) were used in the reaction. After degassing, the reaction was heated to 280 ºC and held at 280 ºC for 60 min. The product was distributed in equal volume into two 50 mL centrifuge tubes filled with ethanol to 30 mL which was centrifuged at 2000 rcf for 10 min to remove excess reactants. The nanoparticle pellet was dispersed and purified using a mixture of 1:10 toluene and ethanol twice and collected by centrifuging at 8000 rcf for 5 min. The nanoparticles were dispersed in 6 mL of toluene.

For the Ni shelling procedure, 200 µL of the above Fe nanoparticles (~ 5 mg) was dried under a stream of argon in a 3-neck, round-bottom flask. Then, 200 µL of OLAM and 5 mL of ODE were added to the flask and the nanoparticles were dispersed in the mixture *via* sonication. After degassing, Ni-COD (40.0 mg, 0.15 mmol) added in 2 mL of DBE was injected into the reaction. The reaction temperature was increased at a rate of 2.5 ºC/min to 200 ºC and held at 200 ºC for 60 min. The product was transferred to a 50 mL centrifuge tube filled with ethanol to 30 mL which was centrifuged at 8000 rcf for 5 min to remove excess reactants. The nanoparticle pellet was dispersed and purified using ethanol and collected by centrifuging at 12500 rcf for 10 min. The nanoparticles were dispersed in 2 mL of toluene.

Nanoparticle Surface Ligand Exchange. The nanoparticles dispersed in toluene were transferred into aqueous dispersion by surface ligand exchange process using methoxypolyethylene glycol carboxylic acid (PEG-COOH, M.W.=5000). In a typical procedure, 2 mL of the nanoparticle suspension in toluene was added to 10 mL of 1 mg/mL PEG-COOH chloroform solution in a 20 mL scintillation vial. The reaction mixture was capped and stirred overnight. The product was distributed in two 50 mL centrifuge tubes which were filled to 45 mL with hexane and centrifuged at 15,000 rcf for 10 min. The resulting pellet was purified with ethanol/water and collected by

centrifuging at 20,000 rcf for 30 min at 4 ºC. The final product was dispersed in 500 µL of ethanol/water for quantification and characterization.

Instrumentation. Low resolution TEM images were captured using a JEOL JEM-1011 microscope with an accelerating voltage of 100 kV. HAADF-STEM images were acquired using the JEM-ARM200F microscope equipped with cold field emission gun and double aberration correctors at the accelerating voltage of 200 kV. The inner and outer collection angles for HAADF images were 67 and 275 mrad, respectively. The spatial resolution of HAADF images was 0.8 Å. The 2D EELS mapping of Fe L-edge and Ni L-edge was carried out using a Gatan energy-loss spectrometer at an accelerating voltage of 200 kV and a beam convergence semi-angle of 21.2 mrad. Dispersion of 0.25 eV/channel was used to simultaneously acquire Fe L-edge and Ni L-edge, as well as O K-edge. The dual-EELS mode was adopted for the convenience of correcting zero-loss. The mass concentrations of Ni and Fe were determined using a Thermo Scientific iCAP Q ICP-MS. XRD patterns were collected on Rigaku Ultima III X-ray diffractometer in a parallel beam geometry. Copper anode x-ray tube was used as a radiation source and diffracted beam monochromator was employed to remove fluorescence background. Samples were deposited on a zero diffraction Silicon plates (MTI Corp., CA) and data was collected at 0.07 degrees per minute scan rates in two theta range from 20 to 80 degrees with 0.1 step. The XPS experiments were carried out in an ultrahigh vacuum (UHV) system with base pressures < 5 x 10^{-9} Torr equipped a hemispherical electron energy analyzer (SPECS, PHOIBOS 100) and twin anode X-ray source (SPECS, XR50). Mg K_α (1253.6 eV) radiation was used at 15 kV and 20 mA. The angle between the analyzer and X-ray source is 45^o and photoelectrons were collected along the sample surface normal. The XPS spectra was analyzed and deconvoluted using Casa XPS software.

X-ray Absorption Spectroscopy. The XAS of the samples and the standards were performed at Argonne National Laboratory (APS 12-BM-B). The standards were purchased from commercial vendors. Standards included nickel foil, nickel oxide, alpha and beta nickel hydroxide, alpha and gamma nickel oxyhydroxide, iron foil, iron oxides (FeO, Fe_2O_3, and Fe_3O_4), iron hydroxide, and iron nickel oxide. Samples and standards were deposited onto the Kapton tape and were sealed on top by a layer of Kapton tape. Along with the standards and the samples, metal reference foils for iron and nickel were also ran simultaneously. The data analysis was done through Athena software. All the standards and the samples were calibrated to the respective metal reference foils. The measurements were performed at room temperature in transmission mode (or fluorescence mode with a 13 elements Ge detector). The samples were scanned at the K-edge of Fe (7112 eV) (150 eV below to 800 eV above) and Ni (8333 eV).

Electrochemical Characterization. The CV and CP were performed on a Pine WaveNow 50 potentiostat using a 3-electrode cell setup. In this setup, Au electrode (BASi®) was used to prepare the working electrode while a graphite rod was used as the counter electrode and Ag/AgCl (kept inside a salt bridge containing 3 M NaCl solution) was used as the reference electrode. In all experiments, 1 M KOH was used as the electrolyte solution. The KOH electrolyte was purified using the method reported by Trotochaud *et. al*.[68] Argon gas was continuously bubbled throughout the experiments to remove oxygen formed in the solution.

Catalyst inks were prepared by mixing the nanoparticles with a cationic ionomer at a ratio of 6:1 (g Fe: g ionomer) in ethanol. The ink was subsequently sonicated for 15 min to mix the nanoparticles and the ionomer homogeneously. Approximately 1 µl of the ink was deposited onto the electrode surface (0.02 cm^2) using the dropcast method and was allowed to dry in air. CV was run at a scan rate of 10 mV/s between 0 V to 0.8 V vs Ag/AgCl. The data at 21st cycle was reported.

CP was conducted for 2 h at a current density of 10 mA/cm^2. Potential in reference to Ag/AgCl was converted into RHE by using the following equation: $E_{RHE} = E_{Ag/AgCl} + 0.059 \cdot pH + E^0_{Ag/AgCl}$, where pH is 14 because the measurement was performed in 1 M KOH; $E^0_{Ag/AgCl}$ is 0.21 V for the reference electrode of Ag/AgCl in 3 M NaCl. The iR_u correction was applied to the CV curves obtained from the measurement where i stands for the measured current in unit ampere and R_u is the value of uncompensated resistance. R_u was measured using potentiostatic electrochemical impendance spectroscopy and the R_u values were taken at a frequency of 100 KHz. Calculation for overpotential was done by subtracting the theoretical potential for OER, 1.23 V, from the measured potential vs. RHE. To calculate the current density (j, mA/cm^2), current is normalized to geometric surface area of the Au electrode (0.02 cm^2). Chronopotentiometry was conducted for 2 h at a current density of 10 mA/cm^2.

Supporting Information

Reaction yield and cost estimations; elemental quantifications using electron microscopy; calculation of turn over frequency; TEM images of NiO_x nanoparticles; XPS spectra; TEM images of FeO_x nanoparticles; XAS spectra of Fe and Ni standards; EXAFS region of Fe and Ni; Table of TOF values; CV profiles of NiO_x-NiO_x/FeO_x with PEG-HH_2 ligands, NiO_x-NiO_x/FeO_x-FeO_x and FeO_x-NiO_x/FeO_x.

Author Contribution

JC and LFG designed the experiments and wrote the manuscript. RHM and CCC synthesized the nanocatalysts. PA performed the electrochemical measurement. DS, JZ, and YZ carried out the electron microscopy characterization. BR and SL performed the XAS measurement. XT conducted the XPS measurement. DN obtained the XRD results. All authors contributed to data analysis, manuscript preparation and editing.

Acknowledgement

We thank Drs. Zhen Wang and Jun Li for the helpful discussion of EELS analysis. JC, LFG, RHM, and PA gratefully acknowledge funding support from the National Science Foundation (NSF), Division of Chemical, Bioengineering, Environmental and Transport Systems (CBET) Catalysis program (Award # 1703827). HRTEM and EELS were carried out at Brookhaven National Laboratory (BNL) sponsored by the U.S. Department of Energy (DOE) Basic Energy Sciences (BES) and by the Materials Sciences and Engineering Division under Contract No. DE-SC0012704. ICP-MS measurements were carried out at the Arkansas Mass Spectrometry facility, which is supported by the Arkansas Biosciences Institute. XPS and XRD measurements were performed at the Center for Functional Nanomaterials (CFN), which is a U.S. DOE Office of Science Facility, at BNL under Contract No. DE-SC0012704. XAS measurements were performed at the 12-BM beamline at the Advanced Photon Source, a U.S. DOE Office of Science User Facility operated for the DOE Office of Science by Argonne National Laboratory under Contract DE-AC02-06CH11357.

References

1. Zeng, K.; Zhang, D., Recent progress in alkaline water electrolysis for hydrogen production and applications. *Progress in Energy and Combustion Science* **2010,** *36* (3), 307-326.
2. Carmo, M.; Fritz, D. L.; Mergel, J.; Stolten, D., A comprehensive review on PEM water electrolysis. *International Journal of Hydrogen Energy* **2013,** *38* (12), 4901-4934.
3. Reier, T.; Nong, H. N.; Teschner, D.; Schlögl, R.; Strasser, P., Electrocatalytic Oxygen Evolution Reaction in Acidic Environments – Reaction Mechanisms and Catalysts. *Advanced Energy Materials* **2017,** *7* (1), 1601275-n/a.
4. Ma, Z.; Zhang, Y.; Liu, S.; Xu, W.; Wu, L.; Hsieh, Y.-C.; Liu, P.; Zhu, Y.; Sasaki, K.; Renner, J. N.; Ayers, K. E.; Adzic, R. R.; Wang, J. X., Reaction mechanism for oxygen evolution on RuO2, IrO2, and RuO2@IrO2 core-shell nanocatalysts. *Journal of Electroanalytical Chemistry* **2018,** *819*, 296-305.
5. Reier, T.; Oezaslan, M.; Strasser, P., Electrocatalytic Oxygen Evolution Reaction (OER) on Ru, Ir, and Pt Catalysts: A Comparative Study of Nanoparticles and Bulk Materials. *ACS Catal.* **2012,** *2* (8), 1765-1772.
6. Lee, Y.; Suntivich, J.; May, K. J.; Perry, E. E.; Shao-Horn, Y., Synthesis and Activities of Rutile IrO2 and RuO2 Nanoparticles for Oxygen Evolution in Acid and Alkaline Solutions. *The Journal of Physical Chemistry Letters* **2012,** *3* (3), 399-404.
7. McCrory, C. C.; Jung, S.; Peters, J. C.; Jaramillo, T. F., Benchmarking heterogeneous electrocatalysts for the oxygen evolution reaction. *Journal of the American Chemical Society* **2013,** *135* (45), 16977-16987.
8. Matsumoto, Y.; Sato, E., Electrocatalytic properties of transition metal oxides for oxygen evolution reaction. *Materials Chemistry and Physics* **1986,** *14* (5), 397-426.
9. Man, I. C.; Su, H.-Y.; Calle-Vallejo, F.; Hansen, H. A.; Martínez, J. I.; Inoglu, N. G.; Kitchin, J.; Jaramillo, T. F.; Nørskov, J. K.; Rossmeisl, J., Universality in Oxygen Evolution Electrocatalysis on Oxide Surfaces. *ChemCatChem* **2011,** *3* (7), 1159-1165.
10. Burke, M. S.; Enman, L. J.; Batchellor, A. S.; Zou, S.; Boettcher, S. W., Oxygen Evolution Reaction Electrocatalysis on Transition Metal Oxides and (Oxy)hydroxides: Activity Trends and Design Principles. *Chemistry of Materials* **2015,** *27* (22), 7549-7558.
11. Fabbri, E.; Habereder, A.; Waltar, K.; Kötz, R.; Schmidt, T. J., Developments and perspectives of oxide-based catalysts for the oxygen evolution reaction. *Catalysis Science & Technology* **2014,** *4* (11), 3800-3821.
12. Kim, J. S.; Kim, B.; Kim, H.; Kang, K., Recent Progress on Multimetal Oxide Catalysts for the Oxygen Evolution Reaction. *Advanced Energy Materials* **2018,** *8* (11), 1702774.
13. Burke, M. S.; Zou, S.; Enman, L. J.; Kellon, J. E.; Gabor, C. A.; Pledger, E.; Boettcher, S. W., Revised Oxygen Evolution Reaction Activity Trends for First-Row Transition-Metal (Oxy)hydroxides in Alkaline Media. *The Journal of Physical Chemistry Letters* **2015,** *6* (18), 3737-3742.
14. Gong, M.; Dai, H., A mini review of NiFe-based materials as highly active oxygen evolution reaction electrocatalysts. *Nano Res.* **2015,** *8* (1), 23-39.
15. Dionigi, F.; Strasser, P., NiFe-Based (Oxy)hydroxide Catalysts for Oxygen Evolution Reaction in Non-Acidic Electrolytes. *Advanced Energy Materials* **2016,** *6* (23), 1600621.
16. Tichenor, R. L., Nickel Oxides-Relation Between Electrochemical and Foreign Ion Content. *Industrial & Engineering Chemistry* **1952,** *44* (5), 973-977.

17. Młynarek, G.; Paszkiewicz, M.; Radniecka, A., The effect of ferric ions on the behaviour of a nickelous hydroxide electrode. *Journal of applied electrochemistry* **1984,** *14* (2), 145-149.
18. Corrigan, D. A., The catalysis of the oxygen evolution reaction by iron impurities in thin-film nickel-oxide electrodes. *Journal of the Electrochemical Society* **1987,** *134* (2), 377-384.
19. Trotochaud, L.; Young, S. L.; Ranney, J. K.; Boettcher, S. W., Nickel-iron oxyhydroxide oxygen-evolution electrocatalysts: The role of intentional and incidental iron incorporation. *J. Am. Chem. Soc.* **2014,** *136*, 6744-6753.
20. Klaus, S.; Louie, M. W.; Trotochaud, L.; Bell, A. T., Role of Catalyst Preparation on the Electrocatalytic Activity of Ni1–xFexOOH for the Oxygen Evolution Reaction. *The Journal of Physical Chemistry C* **2015,** *119* (32), 18303-18316.
21. Ahn, H. S.; Bard, A. J., Surface Interrogation Scanning Electrochemical Microscopy of $Ni_{1-x}Fe_xOOH$ ($0 < x < 0.27$) Oxygen Evolving Catalyst: Kinetics of the "fast" Iron Sites. *Journal of the American Chemical Society* **2016,** *138* (1), 313-318.
22. Görlin, M.; Chernev, P.; Ferreira de Araújo, J.; Reier, T.; Dresp, S.; Paul, B.; Krähnert, R.; Dau, H.; Strasser, P., Oxygen Evolution Reaction Dynamics, Faradaic Charge Efficiency, and the Active Metal Redox States of Ni–Fe Oxide Water Splitting Electrocatalysts. *Journal of the American Chemical Society* **2016,** *138* (17), 5603-5614.
23. Görlin, M.; Ferreira de Araújo, J.; Schmies, H.; Bernsmeier, D.; Dresp, S.; Gliech, M.; Jusys, Z.; Chernev, P.; Kraehnert, R.; Dau, H.; Strasser, P., Tracking Catalyst Redox States and Reaction Dynamics in Ni–Fe Oxyhydroxide Oxygen Evolution Reaction Electrocatalysts: The Role of Catalyst Support and Electrolyte pH. *Journal of the American Chemical Society* **2017,** *139* (5), 2070-2082.
24. Li, N.; Bediako, D. K.; Hadt, R. G.; Hayes, D.; Kempa, T. J.; von Cube, F.; Bell, D. C.; Chen, L. X.; Nocera, D. G., Influence of iron doping on tetravalent nickel content in catalytic oxygen evolving films. *Proceedings of the National Academy of Sciences* **2017,** *114* (7), 1486-1491.
25. Stevens, M. B.; Trang, C. D. M.; Enman, L. J.; Deng, J.; Boettcher, S. W., Reactive Fe-Sites in Ni/Fe (Oxy)hydroxide Are Responsible for Exceptional Oxygen Electrocatalysis Activity. *Journal of the American Chemical Society* **2017,** *139* (33), 11361-11364.
26. Corrigan, D. A.; Conell, R. S.; Fierro, C. A.; Scherson, D. A., In-situ Moessbauer study of redox processes in a composite hydroxide of iron and nickel. *The Journal of Physical Chemistry* **1987,** *91* (19), 5009-5011.
27. Guerlou-Demourgues, L.; Fournès, L.; Delmas, C., In Situ 57Fe Mössbauer Spectroscopy Study of the Electrochemical Behavior of an Iron-Substituted Nickel Hydroxide Electrode. *Journal of The Electrochemical Society* **1996,** *143* (10), 3083-3088.
28. Chen, J. Y. C.; Dang, L.; Liang, H.; Bi, W.; Gerken, J. B.; Jin, S.; Alp, E. E.; Stahl, S. S., Operando Analysis of NiFe and Fe Oxyhydroxide Electrocatalysts for Water Oxidation: Detection of Fe^{4+} by Mössbauer Spectroscopy. *Journal of the American Chemical Society* **2015,** *137* (48), 15090-15093.
29. Louie, M. W.; Bell, A. T., An investigation of thin-film Ni–Fe oxide catalysts for the electrochemical evolution of oxygen. *Journal of the American Chemical Society* **2013,** *135* (33), 12329-12337.
30. Klaus, S.; Cai, Y.; Louie, M. W.; Trotochaud, L.; Bell, A. T., Effects of Fe Electrolyte Impurities on Ni(OH)2/NiOOH Structure and Oxygen Evolution Activity. *The Journal of Physical Chemistry C* **2015,** *119* (13), 7243-7254.

31. Steimecke, M.; Seiffarth, G.; Bron, M., In Situ Characterization of Ni and Ni/Fe Thin Film Electrodes for Oxygen Evolution in Alkaline Media by a Raman-Coupled Scanning Electrochemical Microscope Setup. *Analytical Chemistry* **2017,** *89* (20), 10679-10686.
32. Kim, S.; Tryk, D. A.; Antonio, M. R.; Carr, R.; Scherson, D., In situ x-ray absorption fine structure studies of foreign metal ions in nickel hydrous oxide electrodes in alkaline electrolytes. *The Journal of Physical Chemistry* **1994,** *98* (40), 10269-10276.
33. Balasubramanian, M.; Melendres, C. A.; Mini, S., X-ray Absorption Spectroscopy Studies of the Local Atomic and Electronic Structure of Iron Incorporated into Electrodeposited Hydrous Nickel Oxide Films. *The Journal of Physical Chemistry B* **2000,** *104* (18), 4300-4306.
34. Landon, J.; Demeter, E.; İnoğlu, N.; Keturakis, C.; Wachs, I. E.; Vasić, R.; Frenkel, A. I.; Kitchin, J. R., Spectroscopic Characterization of Mixed Fe–Ni Oxide Electrocatalysts for the Oxygen Evolution Reaction in Alkaline Electrolytes. *ACS Catal.* **2012,** *2* (8), 1793-1801.
35. Trześniewski, B. J.; Diaz-Morales, O.; Vermaas, D. A.; Longo, A.; Bras, W.; Koper, M. T. M.; Smith, W. A., In Situ Observation of Active Oxygen Species in Fe-Containing Ni-Based Oxygen Evolution Catalysts: The Effect of pH on Electrochemical Activity. *Journal of the American Chemical Society* **2015,** *137* (48), 15112-15121.
36. Friebel, D.; Louie, M. W.; Bajdich, M.; Sanwald, K. E.; Cai, Y.; Wise, A. M.; Cheng, M.-J.; Sokaras, D.; Weng, T.-C.; Alonso-Mori, R.; Davis, R. C.; Bargar, J. R.; Nørskov, J. K.; Nilsson, A.; Bell, A. T., Identification of Highly Active Fe Sites in (Ni,Fe)OOH for Electrocatalytic Water Splitting. *Journal of the American Chemical Society* **2015,** *137* (3), 1305-1313.
37. Bates, M. K.; Jia, Q.; Doan, H.; Liang, W.; Mukerjee, S., Charge-Transfer Effects in Ni–Fe and Ni–Fe–Co Mixed-Metal Oxides for the Alkaline Oxygen Evolution Reaction. *ACS Catal.* **2016,** *6* (1), 155-161.
38. González-Flores, D.; Klingan, K.; Chernev, P.; Loos, S.; Mohammadi, M. R.; Pasquini, C.; Kubella, P.; Zaharieva, I.; Smith, R. D.; Dau, H., Nickel-iron catalysts for electrochemical water oxidation–redox synergism investigated by in situ X-ray spectroscopy with millisecond time resolution. *Sustainable Energy & Fuels* **2018**.
39. Smith, R. D.; Pasquini, C.; Loos, S.; Chernev, P.; Klingan, K.; Kubella, P.; Mohammadi, M. R.; González-Flores, D.; Dau, H., Geometric distortions in nickel (oxy) hydroxide electrocatalysts by redox inactive iron ions. *Energy & Environmental Science* **2018**.
40. Li, Y.-F.; Selloni, A., Mechanism and Activity of Water Oxidation on Selected Surfaces of Pure and Fe-Doped NiOx. *ACS Catal.* **2014,** *4* (4), 1148-1153.
41. Conesa, J. C., Electronic Structure of the (Undoped and Fe-Doped) NiOOH O2 Evolution Electrocatalyst. *The Journal of Physical Chemistry C* **2016,** *120* (34), 18999-19010.
42. Xiao, H.; Shin, H.; Goddard, W. A., Synergy between Fe and Ni in the optimal performance of (Ni,Fe)OOH catalysts for the oxygen evolution reaction. *Proceedings of the National Academy of Sciences* **2018,** *115* (23), 5872-5877.
43. Kuai, L.; Geng, J.; Chen, C.; Kan, E.; Liu, Y.; Wang, Q.; Geng, B., A Reliable Aerosol-Spray-Assisted Approach to Produce and Optimize Amorphous Metal Oxide Catalysts for Electrochemical Water Splitting. *Angewandte Chemie International Edition* **2014,** *53* (29), 7547-7551.
44. Song, F.; Hu, X., Exfoliation of layered double hydroxides for enhanced oxygen evolution catalysis. *Nat Commun* **2014,** *5*.

45. Deng, J.; Nellist, M. R.; Stevens, M. B.; Dette, C.; Wang, Y.; Boettcher, S. W., Morphology Dynamics of Single-Layered $Ni(OH)_2$/NiOOH Nanosheets and Subsequent Fe Incorporation Studied by in Situ Electrochemical Atomic Force Microscopy. *Nano Letters* **2017**.
46. Dette, C.; Hurst, M. R.; Deng, J.; Nellist, M. R.; Boettcher, S. W., Structural Evolution of Metal (Oxy)hydroxide Nanosheets during the Oxygen Evolution Reaction. *ACS Applied Materials & Interfaces* **2018**.
47. Huang, J.; Han, J.; Wang, R.; Zhang, Y.; Wang, X.; Zhang, X.; Zhang, Z.; Zhang, Y.; Song, B.; Jin, S., Improving Electrocatalysts for Oxygen Evolution Using NixFe3–xO4/Ni Hybrid Nanostructures Formed by Solvothermal Synthesis. *ACS Energy Letters* **2018,** *3* (7), 1698-1707.
48. Candelaria, S. L.; Bedford, N. M.; Woehl, T. J.; Rentz, N. S.; Showalter, A. R.; Pylypenko, S.; Bunker, B. A.; Lee, S.; Reinhart, B.; Ren, Y.; Ertem, S. P.; Coughlin, E. B.; Sather, N. A.; Horan, J. L.; Herring, A. M.; Greenlee, L. F., Multi-Component Fe–Ni Hydroxide Nanocatalyst for Oxygen Evolution and Methanol Oxidation Reactions under Alkaline Conditions. *ACS Catal.* **2017,** *7* (1), 365-379.
49. Hall, D. S.; Lockwood, D. J.; Bock, C.; MacDougall, B. R., Nickel hydroxides and related materials: a review of their structures, synthesis and properties. *Proceedings. Mathematical, Physical, and Engineering Sciences / The Royal Society* **2015,** *471* (2174), 20140792.
50. Gao, M.; Sheng, W.; Zhuang, Z.; Fang, Q.; Gu, S.; Jiang, J.; Yan, Y., Efficient Water Oxidation Using Nanostructured α-Nickel-Hydroxide as an Electrocatalyst. *Journal of the American Chemical Society* **2014,** *136* (19), 7077-7084.
51. Sun, S.; Zeng, H.; Robinson, D. B.; Raoux, S.; Rice, P. M.; Wang, S. X.; Li, G., Monodisperse MFe2O4 (M = Fe, Co, Mn) Nanoparticles. *Journal of the American Chemical Society* **2004,** *126* (1), 273-279.
52. Chen, S.; Si, R.; Taylor, E.; Janzen, J.; Chen, J., Synthesis of Pd/Fe3O4 Hybrid Nanocatalysts with Controllable Interface and Enhanced Catalytic Activities for CO Oxidation. *The Journal of Physical Chemistry C* **2012,** *116* (23), 12969-12976.
53. Balasubramanian, M.; Melendres, C. A.; Mini, S., X-ray absorption spectroscopy studies of the local atomic and electronic structure of iron incorporated into electrodeposited hydrous nickel oxide films. *J. Phys. Chem. B* **2000,** *104*, 4300-4306.
54. Brollo, M. E. F.; López-Ruiz, R.; Muraca, D.; Figueroa, S. J. A.; Pirota, K. R.; Knobel, M., Compact Ag@Fe3O4 Core-shell Nanoparticles by Means of Single-step Thermal Decomposition Reaction. *Scientific Reports* **2014,** *4*, 6839.
55. Hartl, M.; Gillis, R. C.; Daemen, L.; Olds, D. P.; Page, K.; Carlson, S.; Cheng, Y.; Hügle, T.; Iverson, E. B.; Ramirez-Cuesta, A. J.; Lee, Y.; Muhrer, G., Hydrogen adsorption on two catalysts for the ortho- to parahydrogen conversion: Cr-doped silica and ferric oxide gel. *Physical Chemistry Chemical Physics* **2016,** *18* (26), 17281-17293.
56. Chen, J. Y. C.; Miller, J. T.; Gerken, J. B.; Stahl, S. S., Inverse spinel NiFeAlO4 as a highly active oxygen evolution electrocatalyst: promotion of activity by a redox-inert metal ion. *Energy & Environmental Science* **2014,** *7* (4), 1382-1386.
57. Chen, C. L.; Dong, C.-L., X-Ray Spectroscopy Studies of Iron Chalcogenides. In *Superconductors - Materials, Properties and Applications*, Gabovich, A., Ed. InTech: Rijeka, 2012; p Ch. 02.
58. Regan, T. J.; Ohldag, H.; Stamm, C.; Nolting, F.; Lüning, J.; Stöhr, J.; White, R. L., Chemical effects at metal/oxide interfaces studied by x-ray-absorption spectroscopy. *Physical Review B* **2001,** *64* (21), 214422.

59. Chen, T.; Cao, L.; Zhang, W.; Zhang, W.; Han, Y.; Zheng, Z.; Xu, F.; Kurash, I.; Qian, H.; Wang, J. o., Correlation between electronic structure and magnetic properties of Fe-doped ZnO films. *Journal of Applied Physics* **2012,** *111* (12), 123715.
60. Kim, D. H.; Lee, H. J.; Kim, G.; Koo, Y. S.; Jung, J. H.; Shin, H. J.; Kim, J. Y.; Kang, J. S., Interface electronic structures of BaTiO3@X nanoparticles (X= g-Fe_2O_3, Fe_3O_4, a-Fe_2O_3, and Fe) investigated by XAS and XMCD. *Physical Review B* **2009,** *79* (3), 033402.
61. van Aken, P. A.; Liebscher, B., Quantification of ferrous/ferric ratios in minerals: new evaluation schemes of Fe L23electron energy-loss near-edge spectra. *Physics and Chemistry of Minerals* **2002,** *29* (3), 188-200.
62. Tan, H.; Verbeeck, J.; Abakumov, A.; Van Tendeloo, G., Oxidation state and chemical shift investigation in transition metal oxides by EELS. *Ultramicroscopy* **2012,** *116*, 24-33.
63. Chen, J.; Huang, D. J.; Tanaka, A.; Chang, C. F.; Chung, S. C.; Wu, W. B.; Chen, C. T., Magnetic circular dichroism in Fe *2p* resonant photoemission of magnetite. *Physical Review B* **2004,** *69* (8), 085107.
64. Zhao, W.; Li, M.; Chang, C.-Z.; Jiang, J.; Wu, L.; Liu, C.; Moodera, J. S.; Zhu, Y.; Chan, M. H. W., Direct imaging of electron transfer and its influence on superconducting pairing at FeSe/SrTiO₃ interface. *Science Advances* **2018,** *4* (3).
65. Klaus, S.; Cai, Y.; Louie, M. W.; Trotochaud, L.; Bell, A. T., Effects of Fe electrolyte impurities on $Ni(OH)_2$/NiOOH structure and oxygen evolution activity. *J. Phys. Chem. C* **2015,** *119*, 7243-7254.
66. Bau, J. A.; Luber, E. J.; Buriak, J. M., Oxygen Evolution Catalyzed by Nickel–Iron Oxide Nanocrystals with a Nonequilibrium Phase. *ACS Applied Materials & Interfaces* **2015,** *7* (35), 19755-19763.
67. Smith, R. D. L.; Berlinguette, C. P., Accounting for the Dynamic Oxidative Behavior of Nickel Anodes. *Journal of the American Chemical Society* **2016,** *138* (5), 1561-1567.
68. Trotochaud, L.; Young, S. L.; Ranney, J. K.; Boettcher, S. W., Nickel–Iron Oxyhydroxide Oxygen-Evolution Electrocatalysts: The Role of Intentional and Incidental Iron Incorporation. *Journal of the American Chemical Society* **2014,** *136* (18), 6744-6753.